

Functional Additive Incorporation Enhances the Performance of Semi-Transparent Perovskite Solar Cells

Bhavna Sharma, Krishanu Dey,* Mohammad Adil Afroz, Henry J. Snaith, and Soumitra Satapathi*



Cite This: *ACS Energy Lett.* 2025, 10, 5265–5272



Read Online

ACCESS |



Metrics & More

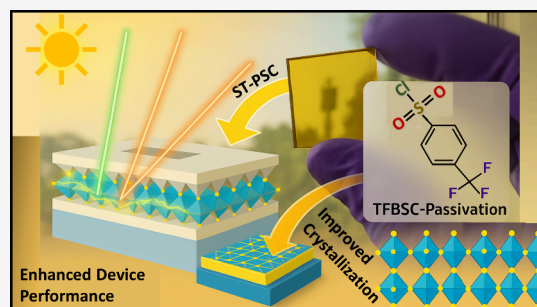


Article Recommendations



Supporting Information

ABSTRACT: Semi-transparent perovskite solar cells (ST-PSCs) have shown great potential in building-integrated photovoltaics. However, the performance of ST-PSCs is still far from achieving their true potential. Herein, a functional additive, [4-(trifluoromethyl)phenyl] sulfonyl chloride (TFBSC), is incorporated into the perovskite precursor solution to regulate the crystallization process and reduce defects in the perovskite films. The addition of TFBSC improves the perovskite film morphology and increases the charge carrier lifetime and photoluminescence quantum efficiency, compared with the control perovskite films. As a result, the champion device modified with TFBSC shows a power conversion efficiency (PCE) of 14.75% with a light utilization efficiency (LUE) of 3.92%, whereas the control device shows PCE and LUE values of 10.71% and 2.96%, respectively. Moreover, the unencapsulated TFBSC-modified device retains ~90% of its initial PCE after 1500 h of storage under ambient conditions (relative humidity of ~30%–40%). These findings could provide new avenues to develop high performance ST-PSCs for smart building applications.



Buildings contribute to 30% of global energy consumption and 26% of total carbon emissions,¹ whereas they account for 33% of the national energy consumption and 20% of the overall carbon emissions in India.² This proportion will continue to increase as living standards are rising. Building integrated photovoltaic (BIPV) technology offers an exciting opportunity to integrate photovoltaics directly into the building envelope and help to achieve net-zero-emission goals.¹ Semi-transparent photovoltaics (STPV) technology has therefore become popular in modern building architecture as the buildings includes glass as a key element for making windows, facades, and skylights.^{3,4} STPV technology is beneficial over conventional silicon (Si) technology because it can generate electricity and allow natural light inside the building.^{5,6} Furthermore, it helps with regard to managing heat dispersion, providing a pleasant and sustainable environment for building architecture.^{7–9} STPVs require an optimum balance between average visible transmittance (AVT) and power conversion efficiency (PCE) for BIPV applications, which can be achieved by reducing the active layer thickness or using wide band-gap photoactive materials.^{10,11} Therefore, light utilization efficiency (LUE), a multiplication of PCE and AVT, is used to assess the overall performance, which balances the contradictory requirements of PCE and AVT in STPVs.^{12,13}

To date, various semiconducting materials has been explored to fabricate semi-transparent solar cells including amorphous Si (a-Si), crystalline Si (c-Si), organic photovoltaics, cadmium telluride, dye-sensitized solar cells, perovskite solar cells (PSCs), etc.^{14–17} PSCs have received considerable attention because of their straightforward fabrication process, availability of resources, lightweight, band gap tunability, flexibility and high photovoltaic performance, compared to the conventional thin film semi-transparent solar cells.^{18–21} In order to meet the aesthetic demand of semi-transparent perovskite solar cells (ST-PSCs), the minimum AVT value must be around 25%.²² Reducing the absorber thickness by lowering precursor concentration can help in achieving required AVT values, but this led to various defects in perovskite layer due to rapid nucleation. As previously reported, it is due to the fast solvent evaporation during annealing process which quickly shift the system toward higher supersaturation states, resulting in an accelerated nucleation rate.^{23–26} Therefore, it is necessary to

Received: August 6, 2025

Revised: September 23, 2025

Accepted: September 29, 2025

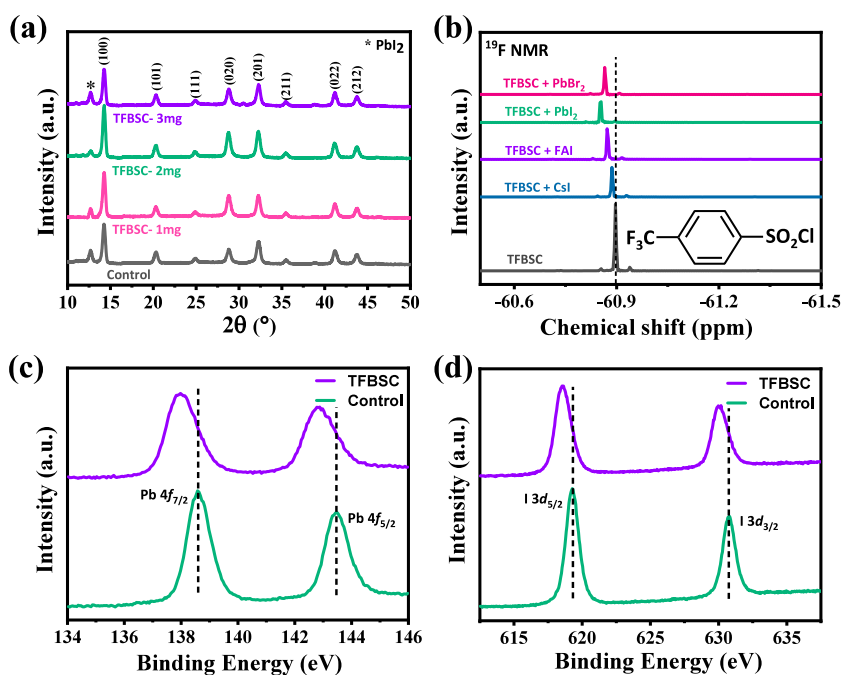


Figure 1. (a) XRD pattern of the perovskite films with or without TFBS; (b) full-range ^{19}F NMR spectra of TFBS with CsI, FAI, PbI_2 , and PbBr_2 (inset shows the molecular structure of TFBS); (c, d) core-level XPS spectra of Pb 4f and I 3d.

regulate the crystallization process to reduce undesired recombination and achieve high-quality perovskite thin films. The most effective method is additive engineering to passivate the defects by achieving a better morphology of perovskite thin films. Generally, small organic molecules and polymers with different functional atoms (such as S, O, N, F) are used for additive engineering.^{27–31} The presence of lone pair electrons on these functional molecules can effectively coordinate with defect sites at grain boundaries and reduce density of defects by regulating the crystallization process during the growth of perovskite thin film.³² Although additive engineering strategies have made substantial advances in traditional perovskite solar cells, understanding of the impact of relevant additives on the performance of ST-PSCs is still limited.

In this study, a small organic molecule [4-(trifluoromethyl)phenyl] sulfonyl chloride (TFBS) was used as an additive in a perovskite precursor solution to regulate the perovskite crystallinity. TFBS contains R-SO₂ and CF₃ functional groups, where S and F may interact with undercoordinated I[−] or PbI_3^- antisites and Pb^{2+} or FA^+ via hydrogen bonding, respectively. This interaction possibly inhibits the formation of these negatively and positively charged defects, thereby resulting in high-quality perovskite thin films. Additionally, our findings also indicate that the introduction of TFBS molecules into the perovskite precursor effectively enhances the photoluminescence quantum efficiency (PLQE), charge carrier lifetime, and charge carrier mobility of perovskite films, which consequently enhances the performance of our ST-PSCs. Moreover, the TFBS molecule exhibits a hydrophobic nature due to the presence of the F group, which enhances the moisture tolerance and long-term stability of ST-PSCs.

X-ray diffraction (XRD) patterns of control and modified perovskite films at different concentrations of TFBS are presented in Figure 1a, to determine the effect of TFBS on their crystallinity and structure. The prominent diffraction peaks at 14.17° and 32.03° respectively correspond to the

(100) and (201) lattice planes of the perovskite, while the peak at 12.8° is attributed to residual PbI_2 . The incorporation of TFBS into the precursor solution increases the intensity of the prominent (100) peak without any shift, suggesting that the incorporation of this molecule does not change the crystal structure of the host lattice. In addition to that, the residual PbI_2 phase was suppressed with the addition of 2 mg/mL TFBS molecules into the precursor, indicating its effective participation in the crystallization process. The ratio of the (100) peak to PbI_2 peak is calculated at each concentration, which yields values of 2.40, 4.05, 5.49, and 2.62 for control, 1, 2, and 3 mg/mL TFBS, respectively. These results further confirm that the optimum concentration of 2 mg/mL leads to the highest (100)/ PbI_2 peak ratio, indicating the effective suppression of PbI_2 and improved perovskite crystallinity. However, the excess concentration of TFBS (3 mg/mL) perturbs the crystallization kinetics, which leads to poor film quality, as previously reported.³³

Field emission scanning electron microscopy (FESEM) is carried out to investigate the surface morphology of the semitransparent perovskite films with and without modifications. Figure S1 shows the FESEM images of control and TFBS-modified semitransparent perovskite films, where the incorporation of TFBS into the perovskite solution is found to significantly increase the average grain size from 156 nm to 214 nm. This enhancement in the grain size is direct evidence of the improved crystallinity and surface morphology of the semitransparent perovskite films after the modification.

Nuclear magnetic resonance (NMR) measurements were performed to gain insights into the effect of incorporating TFBS on the local chemical environment of the host perovskite material. Figure 1b (inset) illustrates the molecular structure of TFBS. This molecule contains two functional groups such as the R-SO₂ and CF₃ group. Here, sulfur (S) atom acts as an electron acceptor due to the presence of electronegative chlorine (Cl) atoms, which withdraw electrons

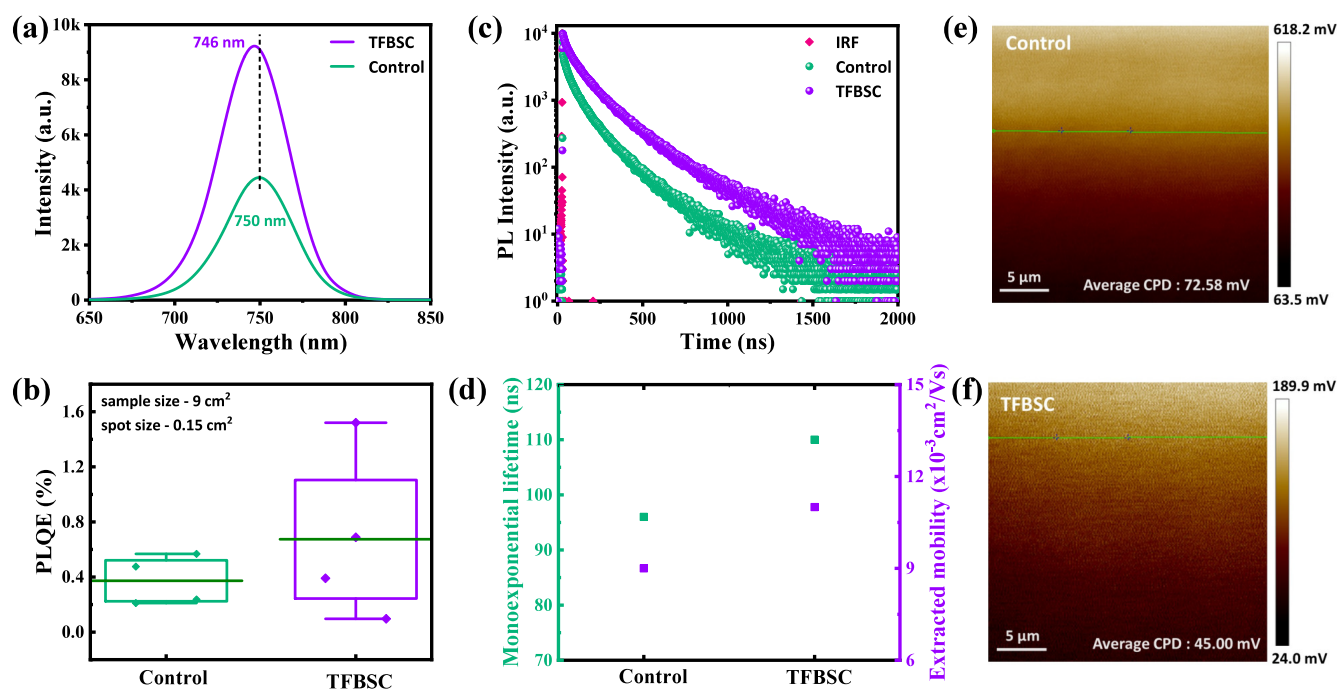


Figure 2. (a) PL spectra of control and TFBS-modified perovskite films; (b) PLQE of control and TFBS-modified perovskite thin films after excitation by 405 nm laser with 1-sun intensity; (c) TRPL spectra of control and TFBS-modified perovskite films; (d) monoexponential lifetime and extracted long-range electron–hole mobility of control and TFBS-modified perovskite films; KPFM measurements of (e) the control and (f) TFBS-modified semitransparent perovskite films.

from the S atom with a partial positive charge on it. Similarly, the carbon (C) atom in the CF_3 group will act as an electron acceptor as the highly electronegative fluorine (F) atoms withdraw electrons from the C atom and leave a partial negative charge on F atoms. As illustrated in Figure 1b, the TFBS peak appearing at -60.89 ppm shows an upfield shift with all perovskite components, which could be attributed to hydrogen bonds formed between the CF_3 group and the Pb^{2+} or FA^+ ions, and the coordination bonds formed between the S atom and undercoordinated I^- ions.³⁴ This could be further corroborated from the ^{13}C NMR spectra of TFBS and other perovskite precursors, as shown in Figure S2. Two prompt peaks appearing at 125.47 and 126.85 ppm correspond to C^a (carbon at the *para* position, with respect to the SO_2Cl group) and $\text{C}^{b,c}$ (carbon at the ortho and meta positions, with respect to the SO_2Cl group). These results reveal that TFBS interacts with the perovskite through its functional groups and effectively reduces defects such as uncoordinated Pb^{2+} ions and cation vacancies.

X-ray photoelectron spectroscopy (XPS) characterizations were performed to further understand the interaction between the perovskite and the TFBS molecule. The survey XPS spectra of control and TFBS-modified perovskite films is shown in Figure S3(a). As shown in Figures 1c and 1d, the Pb 4f and I 3d peaks in the perovskite film exhibit a lower binding energy shift after TFBS modification, compared with unmodified films. The binding energies of Pb 4f_{7/2} and Pb 4f_{5/2} peaks for unmodified perovskite films were observed at 138.5 and 143.4 eV, which shift to 138.0 and 142.8 eV, respectively, after the modifications. Similarly, the binding energies of I 3d_{5/2} and I 3d_{3/2} peaks in the TFBS-modified perovskite films shift from 619.2 and 630.7 eV to 618.5 and 630 eV, respectively. These peak shifts are possibly due to the interaction of S and CF_3 group with undercoordinated I^- and

Pb^{2+} ions, respectively, which helps in stabilizing the PbI_6 octahedra in the perovskite structure.³⁵ Figure S3(b) shows the XPS spectra of C1s with C–C and C–N peaks at 284.8 and 288.2 eV, respectively, in both the modified and unmodified perovskite films. The peak observed at 293 eV, which is absent in the unmodified films, corresponds to the CF_3 (π – π) group, as verified from reported literature.³⁶ Figures S4(a) and S4(b) show the deconvoluted XPS spectra of S 2p and F 1s. The S 2p peak observed at 168 eV is associated with the higher oxidation state of the $-\text{SO}_2-$ group.³⁷ The deconvolution of these S 2p peaks yields components at 168.02 and 169.41 eV, corresponding to S 2p_{3/2} and S 2p_{1/2}, respectively.^{38,39} These deconvolution of these peaks reveals distinct chemical shifts, which we can attribute to the proposed interactions with the undercoordinated Pb^{2+} and I^- sites. Moreover, the F 1s peak is observed at 688.7 eV in the TFBS-modified films. The results from this analysis reveals that these characteristic peaks are absent in the control perovskite film, which supports the successful incorporation of S and F atoms into the TFBS-modified perovskite films.⁴⁰

Next, the impact of TFBS-modification on the charge carrier recombination in perovskite films was studied by using steady-state photoluminescence (PL). Figure 2a illustrates the PL spectra of the control and TFBS-modified perovskite films. A higher PL intensity and a slight blue shift (4 nm) was observed in passivated films, indicating reduced shallow defect density after TFBS modification. This trend is further corroborated by an increase of the average photoluminescence quantum efficiency (PLQE) of control perovskite films from 0.37% to 0.67% after modification by TFBS (Figure 2b).

Moreover, time-resolved photoluminescence (TRPL) spectra were collected to determine the charge carrier lifetimes of control and passivated perovskite thin films. As displayed in Figure 2c, TFBS-modified perovskite films exhibit two decay

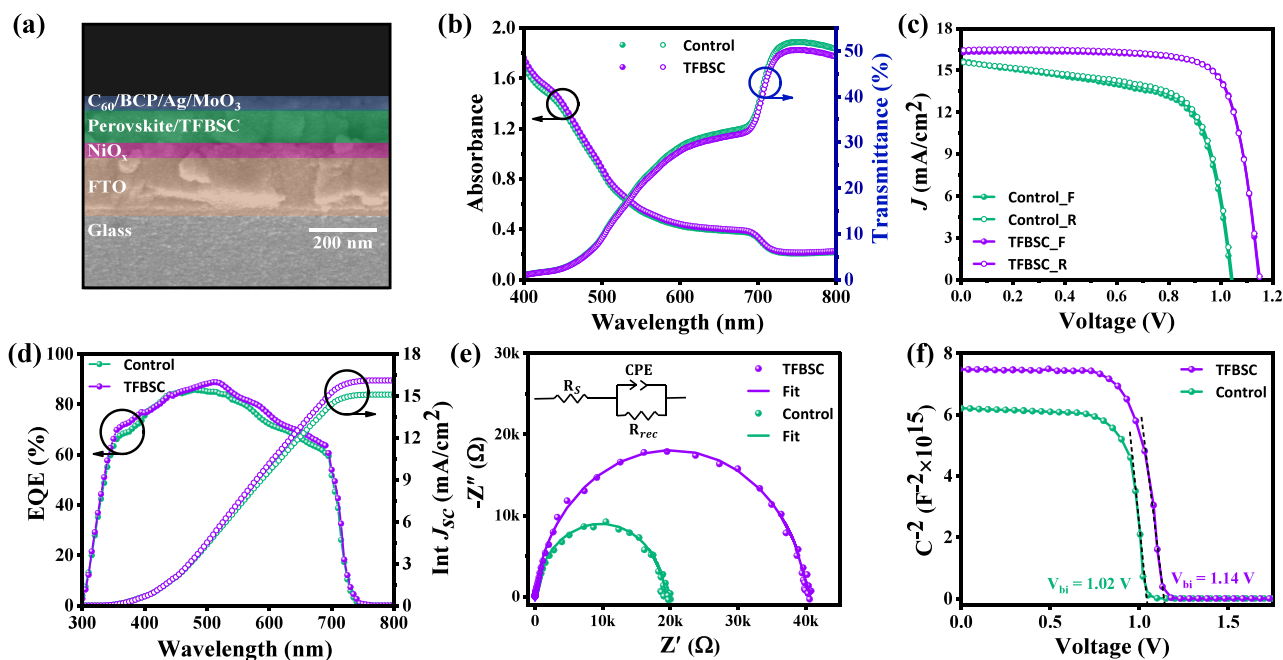


Figure 3. (a) Cross-sectional FESEM of the TFBS-modified device, (b) light absorbance and transmittance spectra, (c) J - V curves, (d) EQE spectra, (e) EIS spectra with an equivalent circuit (inset), and (f) Mott–Schottky plots for control and TFBS-modified ST-PSCs.

components T_1 and T_2 , corresponding to the trap-assisted nonradiative recombination and radiative recombination of free carriers, respectively.⁴¹ Corresponding values of T_1 , T_2 , and T_{ave} are displayed in Table S1. Equation S1 was used to calculate average charge carrier lifetime (T_{ave}) of perovskite thin films and found to be 154.52 ns for control and 189.57 ns for TFBS-modified films. This enhancement in average lifetime is mainly due to the reduced nonradiative recombination losses after TFBS modification. Finally, the long-range mobility of charge carriers in our perovskite films was measured using transient photoconductivity (TPC) measurements.⁴² As shown in Figures S5a and S5b, we observe photoconductivity traces with peak conductivities between 10^{-2} and 10^{-4} S/cm for both the control and TFBS-modified perovskite films. The estimated monoexponential decay lifetime increases from ~ 96 ns to ~ 110 ns after TFBS modification (Figure 2d), which is in agreement with the TRPL results discussed above. By accounting for the early time recombination during the photoexcitation pulse (with a few-nanosecond pulse width), we extract the total (electron + hole) lateral carrier mobility in the perovskite films and present them as a function of the excited carrier density in Figure S6. At the lowest carrier density of $9.4 \times 10^{16} \text{ cm}^{-3}$ (closest to the excitation density under standard 1-sun illumination), the mobility increases from $0.009 \text{ cm}^2/(\text{V s})$ for control to $0.011 \text{ cm}^2/(\text{V s})$ for modified perovskite films (Figure 2d). Furthermore, ultraviolet photoelectron spectroscopy (UPS) was utilized to explore the effect of TFBS incorporation on the energy levels of semi-transparent perovskite films (Figure S7). The conduction band (E_{CB}) and valence band (E_{VB}) positions of both control and TFBS-modified perovskite films were calculated using Equation S2. The results show that control perovskite films have E_{CB} and E_{VB} values of 3.93 and 5.70 eV, respectively, whereas a slight shift is observed in TFBS-modified perovskite films, with $E_{CB} = 3.96$ eV and $E_{VB} = 5.73$ eV. Figure S8a illustrates the energy level alignment for each layer of the corresponding ST-PSC. It can be noted that

the TFBS-modified perovskite film exhibits a significant improvement in energy level alignment with the carrier transport layers, compared to control film, resulting in a reduction in energy loss in ST-PSCs. The incorporation of TFBS in the perovskite solution significantly reduces the energy losses and enhance the collection efficiency of photogenerated carriers in ST-PSCs.⁴³ In addition, Kelvin probe force microscopy (KPFM) measurements were carried out to examine the surface contact potential (V_{CPD}) and the work function difference between the perovskite surface and the KPFM tip. Equation S3 was used to calculate the work function of control and TFBS-modified perovskite films, and corresponding values are presented in Table S2. Control semi-transparent perovskite film shows average V_{CPD} value of 72.58 mV while the TFBS-modified film shows an average V_{CPD} value of 45 mV (see Figures 2e and 2f). Such a decrease in V_{CPD} confirms the passivation effect achieved by the incorporation of TFBS into the perovskite solution.⁴⁴

Figure S8b demonstrates the complete p-i-n architecture of ST-PSCs used in our work: FTO/ NiO_x /perovskite (with or without TFBS)/ C_{60} /BCP/Ag/ MoO_3 . The cross-sectional FESEM image of the device is demonstrated in Figure 3a, showing each layer present in the device. Here, a dielectric-metal-dielectric (DMD) structure with configuration of BCP(8 nm)/Ag(20 nm)/ MoO_3 (5 nm) is used as a top semi-transparent electrode. This DMD configuration demonstrated high transparency, which makes it suitable for BIPV applications.⁴⁵ In order to analyze the AVT of the devices with and without TFBS modification, UV-vis absorption spectroscopy was conducted. Figure 3b shows the absorbance and transmittance spectra of the ST-PSCs, which remain almost the same after the TFBS modification. The AVT of the devices were calculated using eq S4, and the values were found to be 27.69 and 26.58% for control and modified devices, respectively. This shows that the incorporation of the TFBS molecule in the perovskite precursor does not affect the AVT of the devices. The band gap of the fabricated ST-

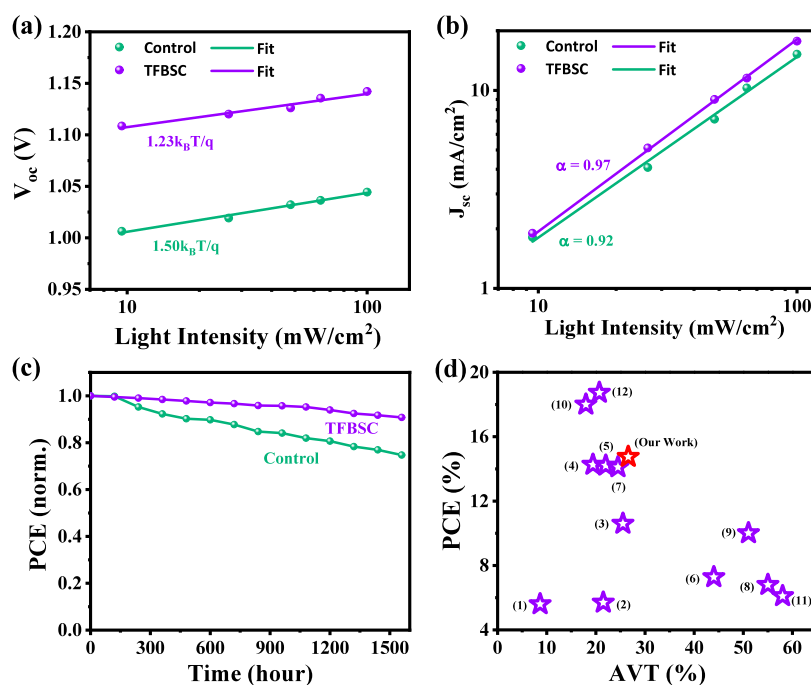


Figure 4. Light-intensity-dependent variation of (a) V_{oc} ; (b) J_{sc} in ST-PSCs; (c) PCE variation of control and TFBS-modified ST-PSCs stored at room temperature, 30% RH for 1500 h; and (d) comparison of our work with recently reported literature in PCE versus AVT.

PSCs with transparent electrode is extracted using Figure S9 and found to be 1.77 eV. This value of band gap is higher than observed in PL emission (~ 1.66 eV), which can be attributed to the defect-mediated recombination and the presence of band-tail states near the band edge, enabling radiative recombination at energies below the actual band edge.^{46–48} In order to determine the optimal concentration of TFBS modification in ST-PSCs, devices were fabricated by using concentrations of 1, 2, and 3 mg/mL. Figure S10 illustrates the J – V curves for the control and different TFBS concentrations under AM 1.5 irradiation. The unmodified device showed a maximum PCE of 10.71% with a V_{oc} of 1.04 V, J_{sc} of 15.17 mA/cm^2 , and fill factor (FF) of 67.5%, whereas the device treated with 2 mg/mL TFBS achieved a maximum PCE of 14.75%, accompanied by a V_{oc} of 1.15 V, J_{sc} of 16.43 mA/cm^2 , and FF of 78.2%. Table S3 summarizes the detailed photovoltaic parameters of ST-PSCs with varying TFBS concentrations. The J – V curves of devices under forward and reverse scan conditions are illustrated in Figure 3c, and the corresponding parameters are summarized in Table S4. Moreover, the external quantum efficiency (EQE) spectrum was recorded for both the control and modified ST-PSC devices (Figure 3d). Integrated J_{sc} values obtained from the EQE spectrum are closely aligned with the J_{sc} values determined by J – V curve measurements. Figure S11 shows the operational stability of the ST-PSCs under continuous illumination at maximum power points (MPPs). The champion device exhibits a steady-state output PCE of 14.96% with a stable J_{sc} of 16.30 mA/cm^2 at MPPs, which closely aligns with the values calculated by the J – V curves. By combining the PCE and AVT values, we calculate the LUE for the control and TFBS-modified devices as 2.96% and 3.92%, respectively, thereby indicating higher performance for BIPV applications. Figure S12 shows the statistical distribution of performance parameters for control and TFBS-modified (15 devices) to examine the reproducibility of ST-PSCs. It

was observed that the TFBS-modified devices exhibit significantly lower deviations in PCE, V_{oc} , J_{sc} , FF, AVT, and LUE, compared to control devices.

The interfacial charge carrier recombination dynamics within the ST-PSCs were also investigated by using electrochemical impedance spectroscopy (EIS). Figure 3e shows the Nyquist plots and corresponding equivalent circuit diagrams for control and TFBS-modified devices. The series resistance (R_s) and recombination resistance (R_{rec}) were calculated by fitting the Nyquist plots, and their values are listed in Table S5. A significant increase in R_{rec} was observed after TFBS modification. The control device shows the R_{rec} value of 19.18 $\text{K}\Omega$, whereas the value increased to 40.16 $\text{K}\Omega$ after the modification, indicating reduced nonradiative recombination losses in the modified devices.⁴⁹ Moreover, the R_s values for the control and TFBS-modified devices were 0.602 and 0.481 $\text{K}\Omega$, respectively. The decrease in R_s value may be attributed to reduced contact resistance and enhanced charge collection after the TFBS passivation, which ultimately increases the FF of the solar cells.

Furthermore, capacitance–voltage (C – V) measurements were carried out to investigate the mechanism responsible for the improvements in V_{oc} and FF with the introduction of TFBS. The values of built-in potential (V_{bi}) were calculated using Equation S5. As illustrated in the Mott–Schottky plots (Figure 3f), the V_{bi} value for the TFBS-modified device is 1.14 V, which is greater than that of the control device (1.02 V). A higher V_{bi} value led to an improved driving force for the separation of photoexcited charge carriers, which ultimately results in better photovoltaic performance in TFBS-modified devices.

Figures 4a and 4b) displayed the J – V characteristics of ST-PSCs under varied light intensity. Equations S6 and S7 show the linear relationship of J_{sc} and V_{oc} with light intensity, which further clarifies the charge-carrier recombination mechanism in ST-PSCs. Here, $\frac{nk_B T}{q}$ is the value obtained by the slope in

Figure 4a, where n is the ideality factor attributed to the defect-assisted recombination.⁵⁰ Usually, an n value close to 1 indicates less defect-aided recombination.⁵¹ TFBCS-modified device exhibits a significantly lower value of n (1.23), compared to the control device (1.50), indicating effective suppression of nonradiative recombination losses in ST-PSCs. Figure 4b illustrates the linear relationship of J_{sc} with the light intensity. The value of α is closer to 1 for TFBCS, compared to unmodified devices, indicating that bimolecular recombination has been suppressed, which promotes efficient transfer of the charge carriers to the charge-transport layer.⁵² Furthermore, dark J - V measurements were performed to evaluate charge carrier shunting caused by defects in ST-PSCs. As shown in Figure S13, the control device exhibited a higher leakage current, whereas devices modified with TFBCS showed a significantly reduced leakage current, indicating less trap density. This results in greater charge extraction efficiency and less trap-assisted recombination, which led to improved V_{oc} .⁵³ Moreover, the unencapsulated TFBCS-modified devices retain almost 90% of their initial PCE after 1500 h of storage in a relative humidity of 30%–40%, whereas the control device decreases to 70% (Figure 4c). This enhancement in ambient stability could be attributed to the hydrophobic nature of the TFBCS additives, where the measured water contact angle of the control perovskite film increases from 33.36° to 51.69° after the incorporation of TFBCS in the perovskite precursor solution (Figure S14). Figure 4d shows the PCE versus AVT plot of the ST-PSCs, demonstrating a comparison of our work with recent literatures. A detailed comparison of all of the performance parameters was shown in Table S6, reflecting one of the highest LUE values reported.

In conclusion, a novel small organic molecule TFBCS has been used as an additive into the perovskite precursor solution, which regulates the perovskite crystallization, resulting in high-quality films with reduced defect density. This is manifested in the increased PLQE, charge carrier lifetime, and long-range mobility as observed in the perovskite film after modification by TFBCS. Consequently, TFBCS-modified devices showed an improved PCE and LUE of 14.75% and 3.92%, which are significantly higher than the values for the control devices (10.71% and 2.96% respectively). Furthermore, the TFBCS-modified devices exhibited improved ambient stability, compared to the control devices, due to the hydrophobic nature and superior quality of TFBCS-modified perovskite thin films. This work provides new insights into the influence of additive engineering on the crystallization process and defect suppression for developing high-efficiency and stable ST-PSCs for BIPV applications.

■ ASSOCIATED CONTENT

SI Supporting Information

The Supporting Information is available free of charge at <https://pubs.acs.org/doi/10.1021/acseenergylett.5c02494>.

Experimental details, theoretical calculations, Figures S1–S14, and Tables S1–S6 (PDF)

■ AUTHOR INFORMATION

Corresponding Authors

Soumitra Satapathi – Department of Physics, Indian Institute of Technology Roorkee, Roorkee, Uttarakhand 247667, India; Center for Sustainable Energy, Indian Institute of Technology Roorkee, Roorkee, Uttarakhand 247667, India;

orcid.org/0000-0001-9218-3796;

Email: soumitra.satapathi@ph.iitr.ac.in

Krishanu Dey – Clarendon Laboratory, Department of Physics, University of Oxford, Oxford OX1 3PU, United Kingdom; orcid.org/0000-0003-3469-6184;
Email: krishanu.dey@physics.ox.ac.uk

Authors

Bhavna Sharma – Department of Physics, Indian Institute of Technology Roorkee, Roorkee, Uttarakhand 247667, India; orcid.org/0000-0002-3124-3051

Mohammad Adil Afroz – Department of Physics, Indian Institute of Technology Roorkee, Roorkee, Uttarakhand 247667, India; orcid.org/0000-0002-0411-8714

Henry J. Snaith – Clarendon Laboratory, Department of Physics, University of Oxford, Oxford OX1 3PU, United Kingdom; orcid.org/0000-0001-8511-790X

Complete contact information is available at: <https://pubs.acs.org/10.1021/acseenergylett.5c02494>

Notes

The authors declare no competing financial interest.

■ ACKNOWLEDGMENTS

This work is financially supported by the Intensification of Research in High Priority Areas (Grant No. SER-1852-PHY) and Ministry of Education (MoE) program of India. K.D. acknowledges the financial support of John Fell Fund Grant (Grant Code: DTD00240) from Oxford University Press and Engineering and Physical Sciences Research Council (Project Reference: EP/V061747/1).

■ REFERENCES

- Jaysawal, R. K.; Chakraborty, S.; Elangovan, D.; Padmanaban, S. Concept of net zero energy buildings (NZEB)—A literature review. *Cleaner Eng. Technol.* **2022**, *11*, 100582.
- Behal, D. *How Efficient Buildings Can Help India Meet Its Climate Goals*; IndiaSpend, 2023. Available via the Internet at: <https://www.indiaspend.com/climate-change/how-efficient-buildings-can-help-india-meet-its-climate-goals-877297> (accessed September 30, 2023).
- Kumar, P.; You, S.; Vomiero, A. Recent Progress in Materials and Device Design for Semitransparent Photovoltaic Technologies. *Adv. Energy Mater.* **2023**, *13* (39), 2301555.
- Sharma, B.; Garai, R.; Afroz, M. A.; Sharma, T.; Choudhary, S.; Singh, R. K.; Satapathi, S. Enhancing Light Utilization Efficiency of Semi-Transparent Perovskite Solar Cells via Tailored Interfacial Engineering. *Adv. Energy Mater.* **2024**, *14* (39), 2402473.
- Martin-Chivelet, N.; Kapsis, K.; Wilson, H. R.; Delisle, V.; Yang, R.; Olivieri, L.; Polo, J.; Eisenlohr, J.; Roy, B.; Maturi, L.; et al. Building-Integrated Photovoltaic (BIPV) products and systems: A review of energy-related behavior. *Energy Build.* **2022**, *262*, 111998.
- Sharma, B.; Satapathi, S. Semi-Transparent Perovskite Solar Cells for Building Integrated Photovoltaics Application. *Adv. Mater. Technol.* **2025**, *10* (16), e00434.
- Cannavale, A.; Hörantner, M.; Eperon, G. E.; Snaith, H. J.; Fiorito, F.; Ayr, U.; Martellotta, F. Building integration of semi-transparent perovskite-based solar cells: Energy performance and visual comfort assessment. *Appl. Energy* **2017**, *194*, 94–107.
- Wang, M.; Cao, F.; Wang, M.; Deng, K.; Li, L. Intermediate-Adduct-Assisted Growth of Stable CsPbI₂Br Inorganic Perovskite Films for High-Efficiency Semitransparent Solar Cells. *Adv. Mater.* **2021**, *33* (10), 2006745.
- Wang, D.; Liu, H.; Li, Y.; Zhou, G.; Zhan, L.; Zhu, H.; Lu, X.; Chen, H.; Li, C.-Z. High-performance and eco-friendly semi-transparent organic solar cells for greenhouse applications. *Joule* **2021**, *5* (4), 945–957.

- (10) Dou, Y.; Liu, Z.; Wu, Z.; Liu, Y.; Li, J.; Leng, C.; Fang, D.; Liang, G.; Xiao, J.; Li, W.; et al. Self-augmented ion blocking of sandwiched 2D/1D/2D electrode for solution processed high efficiency semitransparent perovskite solar cell. *Nano Energy* **2020**, *71*, 104567.
- (11) Upama, M. B.; Wright, M.; Elumalai, N. K.; Mahmud, M. A.; Wang, D.; Xu, C.; Uddin, A. High-Efficiency Semitransparent Organic Solar Cells with Non-Fullerene Acceptor for Window Application. *ACS Photonics* **2017**, *4* (9), 2327–2334.
- (12) Cui, X.; Li, X.; Wang, Z.; Li, Z.; Chen, X.; Tang, J.; Feng, X.; La, S.; Chen, J.; Zhang, Z.; et al. MoO₃/Au/Ag/MoO₃ multilayer transparent electrode enables high light utilization of semitransparent perovskite solar cells. *Device* **2025**, *3*, 100558.
- (13) Sharma, B.; Afroz, M. A.; Sharma, T.; Saliba, M.; Satapathi, S. Buried Interfacial Passivation in NiOx-Based Inverted Semi-Transparent Perovskite Solar Cells. *Small* **2025**, *21* (22), 2502654.
- (14) Park, J.; Dao, V. A.; Kim, S.; Pham, D. P.; Kim, S.; Le, A. H. T.; Kang, J.; Yi, J. High Efficiency Inorganic/Inorganic Amorphous Silicon/Heterojunction Silicon Tandem Solar Cells. *Sci. Rep.* **2018**, *8* (1), 15386.
- (15) Yang, K.-Y.; Lee, W.; Jeon, J.-Y.; Ha, T.-J.; Kim, Y.-H. Controlling the visibility of embedded silicon solar cells in building-integrated photovoltaic windows using surface structure modification and metal-oxide back coating. *Sol. Energy* **2020**, *197*, 99–104.
- (16) Yan, F.; Noble, J.; Peltola, J.; Wicks, S.; Balasubramanian, S. Semitransparent OPV modules pass environmental chamber test requirements. *Sol. Energy Mater. Sol. Cells* **2013**, *114*, 214–218.
- (17) Liu, X.; Yang, H.; Wang, C.; Shen, C.; Bo, R.; Hinkle, L.; Wang, J. Semi-experimental investigation on the energy performance of photovoltaic double skin façade with different façade materials. *Energy* **2024**, *295*, 131049.
- (18) Wong, V. K.; Ho, J. K. W.; Wong, W. W. H.; So, S. K. Semitransparent solar cells: strategies for maximum power output in cities. *Energy Environ. Sci.* **2025**, *18*, 579.
- (19) Upama, M. B.; Wright, M.; Elumalai, N. K.; Mahmud, M. A.; Wang, D.; Chan, K. H.; Xu, C.; Haque, F.; Uddin, A. High performance semitransparent organic solar cells with 5% PCE using non-patterned MoO₃/Ag/MoO₃ anode. *Curr. Appl. Phys.* **2017**, *17* (2), 298–305.
- (20) Sharma, B.; Tailor, N. K.; Chauhan, R.; Ghosh, K.; Satapathi, S. Structure-Dependent Photophysical and Thermal Properties of Lead-Free Antimony Perovskites. *Energy Fuels* **2025**, *39* (15), 7467–7475.
- (21) Afroz, M. A.; Sharma, B.; Sharma, R. K.; Gupta, R. K.; Sengupta, A.; Srivastava, S. K.; Satapathi, S. Solution processable perovskite-hybrid heterojunction silicon 4T tandem solar cells. *Mater. Today Adv.* **2025**, *25*, 100558.
- (22) Han, S.; Deng, Y.; Han, W.; Ren, G.; Song, Z.; Liu, C.; Guo, W. Recent advances of semitransparent organic solar cells. *Sol. Energy* **2021**, *225*, 97–107.
- (23) Ran, C.; Xu, J.; Gao, W.; Huang, C.; Dou, S. Defects in metal triiodide perovskite materials towards high-performance solar cells: origin, impact, characterization, and engineering. *Chem. Soc. Rev.* **2018**, *47* (12), 4581–4610.
- (24) Lee, J.-W.; Bae, S.-H.; De Marco, N.; Hsieh, Y.-T.; Dai, Z.; Yang, Y. The role of grain boundaries in perovskite solar cells. *Mater. Today Energy* **2018**, *7*, 149–160.
- (25) Garai, R.; Sharma, B.; Afroz, M. A.; Choudhary, S.; Sharma, T.; Metcalf, L.; Tailor, N. K.; Iyer, P. K.; Mohite, A. D.; Satapathi, S. High-Efficiency Semitransparent Perovskite Solar Cells Enabled by Controlling the Crystallization of Ultrathin Films. *ACS Energy Lett.* **2024**, *9* (6), 2936–2943.
- (26) Knight, A. J.; Herz, L. M. Preventing phase segregation in mixed-halide perovskites: a perspective. *Energy Environ. Sci.* **2020**, *13* (7), 2024–2046.
- (27) Li, X.; Zhang, W.; Wang, Y.-C.; Zhang, W.; Wang, H.-Q.; Fang, J. In-situ cross-linking strategy for efficient and operationally stable methylammonium lead iodide solar cells. *Nat. Commun.* **2018**, *9* (1), 3806.
- (28) Zhang, J.; Li, Z.; Guo, F.; Jiang, H.; Yan, W.; Peng, C.; Liu, R.; Wang, L.; Gao, H.; Pang, S.; et al. Thermally Crosslinked F-rich Polymer to Inhibit Lead Leakage for Sustainable Perovskite Solar Cells and Modules. *Angew. Chem., Int. Ed.* **2023**, *62* (31), e202305221.
- (29) Ren, N.; Wang, P.; Jiang, J.; Li, R.; Han, W.; Liu, J.; Zhu, Z.; Chen, B.; Xu, Q.; Li, T.; et al. Multifunctional Additive CdAc₂ for Efficient Perovskite-Based Solar Cells. *Adv. Mater.* **2023**, *35* (32), 2211806.
- (30) Wu, Y.; Xu, G.; Xi, J.; Shen, Y.; Wu, X.; Tang, X.; Ding, J.; Yang, H.; Cheng, Q.; Chen, Z.; et al. In situ crosslinking-assisted perovskite grain growth for mechanically robust flexible perovskite solar cells with 23.4% efficiency. *Joule* **2023**, *7* (2), 398–415.
- (31) Zhang, Y.; Xing, Z.; Fan, B.; Ni, Z.; Wang, F.; Hu, X.; Chen, Y. Uncovering Aging Chemistry of Perovskite Precursor Solutions and Anti-aging Mechanism of Additives. *Angew. Chem., Int. Ed.* **2023**, *135* (8), DOI: 10.1002/ange.202215799.
- (32) Wu, T.; Wang, P.; Zheng, L.; Zhao, Y.; Hua, Y. Perovskite Crystallization and Hot Carrier Dynamics Manipulation Enables Efficient and Stable Perovskite Solar Cells with 25.32% Efficiency. *Adv. Energy Mater.* **2024**, *14* (24), 2400078.
- (33) Adil Afroz, M.; Ghimire, N.; Reza, K. M.; Bahrami, B.; Bobba, R. S.; Gurung, A.; Chowdhury, A. H.; Iyer, P. K.; Qiao, Q. Thermal Stability and Performance Enhancement of Perovskite Solar Cells Through Oxalic Acid-Induced Perovskite Formation. *ACS Appl. Energy Mater.* **2020**, *3* (3), 2432–2439.
- (34) Yi, Z.; Zhang, W.; Xiong, Y.; Xiao, B.; Jiang, Q.; Luo, Y.; Li, X.; Yang, J. Significant Efficiency and Stability Enhancement of Flexible Perovskite Solar Cells Combining with Multifunctional Effects of a Natural Spice. *Adv. Funct. Mater.* **2024**, *34* (9), 2310194.
- (35) Zhou, J.; Li, M.; Wang, S.; Tan, L.; Liu, Y.; Jiang, C.; Zhao, X.; Ding, L.; Yi, C. 2-CF₃-PEAI to eliminate Pb⁰ traps and form a 2D perovskite layer to enhance the performance and stability of perovskite solar cells. *Nano Energy* **2022**, *95*, 107036.
- (36) Gunn, F.; Ghosh, P.; Maciejczyk, M.; Cameron, J.; Nordlund, D.; Krishnamurthy, S.; Tuttle, T.; Skabara, P.; Robertson, N.; Ivaturi, A. Understanding the dopant induced effects on SFX-MeOTAD for perovskite solar cells: a spectroscopic and computational investigation. *J. Mater. Chem. C* **2021**, *9* (45), 16226–16239.
- (37) Tudino, T. C.; Nunes, R. S.; Mandelli, D.; Carvalho, W. A. Influence of Dimethylsulfoxide and Dioxygen in the Fructose Conversion to 5-Hydroxymethylfurfural Mediated by Glycerol's Acidic Carbon. *Front. Chem.* **2020**, *8*, 263.
- (38) Deblomme-Chouvy, C.; Haskouri, S.; Cachet, H. Study by XPS of the chlorination of proteins aggregated onto tin dioxide during electrochemical production of hypochlorous acid. *Appl. Surf. Sci.* **2007**, *253* (12), 5506–5510.
- (39) Schick, G. A.; Sun, Z. Spectroscopic Characterization of Sulfonyl Chloride Immobilization on Silica. *Langmuir* **1994**, *10* (9), 3105–3110.
- (40) Lin, W.; Wu, J.; Tian, J.; Lin, Y.; Yang, P.; Huang, Y.; Jiang, X.; Gao, L.; Wang, Y.; Sun, W.; et al. Synergistic Effect of 2-(Trifluoromethyl) Benzimidazole on the Stability and Performance of Perovskite Solar Cells. *ACS Appl. Mater. Interfaces* **2023**, *15* (30), 36468–36476.
- (41) Wu, Z.; Jiang, M.; Liu, Z.; Jamshaid, A.; Ono, L. K.; Qi, Y. Highly Efficient Perovskite Solar Cells Enabled by Multiple Ligand Passivation. *Adv. Energy Mater.* **2020**, *10* (10), 1903696.
- (42) Lim, J.; Kober-Czerny, M.; Lin, Y.-H.; Ball, J. M.; Sakai, N.; Duijnste, E. A.; Hong, M. J.; Labram, J. G.; Wenger, B.; Snaith, H. J. Long-range charge carrier mobility in metal halide perovskite thin-films and single crystals via transient photo-conductivity. *Nat. Commun.* **2022**, *13* (1), 4201.
- (43) Xie, L.; Chen, J.; Vashishtha, P.; Zhao, X.; Shin, G. S.; Mhaisalkar, S. G.; Park, N.-G. Importance of Functional Groups in Cross-Linking Methoxysilane Additives for High-Efficiency and Stable Perovskite Solar Cells. *ACS Energy Letters* **2019**, *4* (9), 2192–2200.
- (44) Emshadi, K.; Ghimire, N.; Gurung, A.; Bahrami, B.; Pathak, R.; Bobba, R. S.; Lamsal, B. S.; Rahman, S. I.; Chowdhury, A. H.; Chen,

K.; et al. Tailoring the Grain Boundaries of Wide-Bandgap Perovskite Solar Cells by Molecular Engineering. *Solar RRL* **2020**, *4* (12), 2000384.

(45) Boopathi, K. M.; Hanmandlu, C.; Singh, A.; Chen, Y.-F.; Lai, C. S.; Chu, C. W. UV- and NIR-Protective Semitransparent Smart Windows Based on Metal Halide Solar Cells. *ACS Applied Energy Materials* **2018**, *1* (2), 632–637.

(46) Saba, M.; Cadelano, M.; Marongiu, D.; Chen, F.; Sarritzu, V.; Sestu, N.; Figus, C.; Aresti, M.; Piras, R.; Geddo Lehmann, A.; et al. Correlated electron-hole plasma in organometal perovskites. *Nat. Commun.* **2014**, *5* (1), 5049.

(47) Sidhik, S.; Metcalf, L.; Li, W.; Kodalle, T.; Dolan, C. J.; Khalili, M.; Hou, J.; Mandani, F.; Torma, A.; Zhang, H.; et al. Two-dimensional perovskite templates for durable, efficient formamidinium perovskite solar cells. *Science* **2024**, *384* (6701), 1227–1235.

(48) Garai, R.; Afroz, M. A.; Gupta, R. K.; Iyer, P. K. Efficient Trap Passivation of MAPbI₃ via Multifunctional Anchoring for High-Performance and Stable Perovskite Solar Cells. *Adv. Sustainable Syst.* **2020**, *4* (8), 2000078.

(49) Garai, R.; Gupta, R. K.; Hossain, M.; Iyer, P. K. Surface recrystallized stable 2D-3D graded perovskite solar cells for efficiency beyond 21%. *J. Mater. Chem. A* **2021**, *9* (46), 26069–26076.

(50) Azmi, R.; Hadmojo, W. T.; Sinaga, S.; Lee, C.-L.; Yoon, S. C.; Jung, I. H.; Jang, S.-Y. High-Efficiency Low-Temperature ZnO Based Perovskite Solar Cells Based on Highly Polar, Nonwetting Self-Assembled Molecular Layers. *Adv. Energy Mater.* **2018**, *8* (5), 1701683.

(51) Su, Y.; Yang, J.; Liu, G.; Sheng, W.; Zhang, J.; Zhong, Y.; Tan, L.; Chen, Y. Acetic Acid-Assisted Synergistic Modulation of Crystallization Kinetics and Inhibition of Sn²⁺ Oxidation in Tin-Based Perovskite Solar Cells. *Adv. Funct. Mater.* **2022**, *32* (12), 2109631.

(52) Huang, Z.; Hu, X.; Liu, C.; Tan, L.; Chen, Y. Nucleation and Crystallization Control via Polyurethane to Enhance the Bendability of Perovskite Solar Cells with Excellent Device Performance. *Adv. Funct. Mater.* **2017**, *27* (41), 1703061.

(53) Xia, Y.; Ran, C.; Chen, Y.; Li, Q.; Jiang, N.; Li, C.; Pan, Y.; Li, T.; Wang, J.; Huang, W. Management of perovskite intermediates for highly efficient inverted planar heterojunction perovskite solar cells. *J. Mater. Chem. A* **2017**, *5* (7), 3193–3202.